Chemical Engineering Journal 525 (2025) 170043

Contents lists available at ScienceDirect

Chemical Engineering Journal

journal homepage: www.elsevier.com/locate/cej

MXene triggers room-temperature 4D printing of advanced ionic hydrogels for sensitive electronic skin

Qinglong He [a,1], Chendong Zhao [a,1], Yuanjie Jiang [a], Jimei Liu [a], Xinyu Liu [a], Rui Jia [a], Cheng Yang [b], Mengzhou Liao [a], Yan Zhao [a], Desheng Kong [b], Valeria Nicolosi [c], Caofeng Pan [d], Chuanfang Zhang [a,*]

[a] College of Materials Science & Engineering, Sichuan University, Chengdu, Sichuan, 610065, China
[b] College of Engineering and Applied Sciences, Nanjing University, Nanjing, Jiangsu, 210021, China
[c] School of Chemistry, Centre for Research on Adaptive Nanostructures and Nanodevices (CRANN) & Advanced Materials and BioEngineering Research (AMBER), Trinity College Dublin, Dublin, Dublin 2, Ireland
[d] Institute of Atomic Manufacturing, International Research Institute for Multidisciplinary Science, Beihang University, Beijing, 100191, China

ARTICLE INFO

Keywords:
4D printing
MXene
Triggering chemistry
Highly entangled networks
Skin sensors

ABSTRACT

3D-printed structured hydrogels hold significant promise for applications in human-machine interfaces, electronic skins, and health monitoring. However, their development is hampered by the inherent conflict between rapid fabrication and slow growth of long-chain polymer, manifesting as low mechanical strength and high hysteresis. Herein, we developed an aqueous interfacial diffusive polymerization (AIDP) strategy by leveraging spatially distributed MXene to trigger the generation of free radicals at room-temperature. This strategy effectively decouples the 3D printing shaping process from the subsequent long-chain growth. The preliminary framework further polymerizes in the initiator bath and develops into a dense, highly-entangled network with time – a technique designated as 4D printing. As a result, highly uniform, resolution hydrogels (~162 μm in width) with large tensile strength (0.73 MPa) and remarkably low hysteresis (< 3 % at 200 % strain) are achieved simultaneously. These enhanced mechanical properties enable stable acquisition of electrical signals when the ion-conductive hydrogel functions as a strain sensor. Furthermore, the hydrogel was integrated into a smart glove, demonstrating real-time, wireless device manipulation through finger-joints-activity signal classification using machine learning algorithms. This work demonstrates significant potential for next-generation flexible electronics and bio-interfaces.

1. Introduction

Hydrogels are indispensable in artificial organs and tissues due to their exotic properties such as biocompatibility [1,2], hydrophilicity [3–5], and flexibility [6–10]. Developing elastic, ionic-conductive hydrogels capable of sensitively monitoring bioelectrical signals is important for the advancement of electronic skin [11,12], brain-machine interfaces [13,14], biomedical implants [15], and tissue regeneration [16], etc. To date, 3D printing of hydrogels has been extensively explored [17–19]. However, these as-printed hydrogels achived by extruding the inks with pre-polymerized network through the nozzle, typically exhibit compromised mechanical strength and large hysteresis that incompatible with the ever-increasing demands on the advanced hydrogels. In other words, balancing precise control over polymer network growth while achieving efficient printing of hydrogels with high-resolution has proven to be quite challenging [20]. To this end, introducing a time dimension into printing—allowing the preliminarily polymerized materials to change their structures over time—so called four dimensional (4D) printing, is expected to revolutionalize the hydrogels with exotic properties. Importantly, 4D printing not only inherits all the advantages of 3D printing, but also enables the printed precursor inks to intentionally alter their shape, properties, or functions over time in response to external stimuli [21].

In recent years, 4D printing of hydrogels has primarily focused on two approaches: vat photopolymerization and direct ink writing (DIW) [22]. The photopolymerization-based 4D printing produces complex

* Corresponding author at: College of Materials Science and Engineering, Sichuan University, Chengdu, China.
E-mail address: chuanfang.zhang@scu.edu.cn (C. Zhang).
[1] These authors contributed equally to this work.

https://doi.org/10.1016/j.cej.2025.170043
Received 10 August 2025; Received in revised form 15 October 2025; Accepted 22 October 2025
Available online 28 October 2025

hydrogels with high resolution [18]. For instance, Dhand et al. recently reported the use of photopolymerization strategy to rapidly solidify the hydrogel shapes and to initiate continuous redox polymerization thereafter, forming highly entangled hydrogel networks [23]. This photopolymerization-based 4D printing effectively resolves the contradiction between the formation of highly entangled networks and the printing speed, nevertheless, issues including narrow selection of suitable inks and the inhomogeneous polymerization during the curing stage greatly limit this strategy from massive application.

Alternatively, DIW-based 4D printing is known for the broad material choices, multi-material printing capability and cost-effective [24]. Nonetheless, due to the structural design and molding method of hydrogel network, this method suffers from lower resolution, poor mechanical stability, and slower printing speed. For example, MXene-based hydrogels can be 4D printed assisted by the thermal stimuli, however, the formation of non-covalent bonds render brittle, unstable physical bridging networks in the hydrogel [25]. By designing physically entangled polymer chains, stretchable and mechanically robust hydrogel structures can be realized [26]. Nevertheless, the printing speed as well as the controllable formation of entangled network remain major challenges. On the other hand, 4D printing of hydrogels in supportive baths has emerged as a new strategy for fabricating hydrogels with complex geometries at high resolution.

Recent advances suggest that diffusion-driven polymerization can overcome these trade-offs. Cai et al. [27] systematically categorized diffusion-enabled bioprinting into “into-ink,” “out-of-ink,” and “within-construct” paradigms, highlighting how directional transport of initiators or activators across interfaces can be harnessed as a design principle rather than treated as a limitation. Building on this concept, Ding et al. [28] demonstrated that diffusive influx of initiators, when coupled with anisotropic crosslinking, enables 4D living-cell constructs with programmed shape morphing. More recently, Lee et al. [29] extended diffusion-activation to thermosets: activators in an embedding bath diffuse into the ink to unmask a dormant Ru catalyst, curing a polymer “skin” in situ.

Therefore, we have integrated our previously proposed unique mechanism of MXene-triggered initiator dissociation [30] with the distinctive printability and extrudability of MXene dispersions [31]., and we propose an AIDP strategy to rapidly 4D printing of elastic hydrogels with ultralow hysteresis. Once the inks (consisted of monomer, crosslinker, thickener and MXene flakes) are extruded into the initiator solution, the initiator rapidly diffuse into the ink and interact with MXene nanosheets, the latter greatly lowers down the decomposition enthalpy of the former, releases abundant free radials ($\cdot SO_4^-$), triggers rapid interfacial polymerization and quickly solidifies the surface of 3D extruded filaments. As a result, the shape and geometry of the extruded filaments are well preserved without disassembling. The junior framework further polymerizes in the initiator bath and develops into a dense, highly-entangled network with time, leading to ionic-conductive (~4 S/m) hydrogels with superior elasticity, low hysteresis (2.93 %), high modulus (0.73 MPa) and self-healing capability, etc. We define the technology of extruding this ink into an initiator solution and subsequently spatially growing and shaping the polymer over time as 4D printing technology. We further demonstrate the application of these 4D printed hydrogels as stretchable strain sensors, offering high sensitivity, long-term stability and minimal electrical hysteresis. We note that such a AIDP-assisted 4D printing strategy imposes less requirements on ink rheology and thixotropy, and eliminates issues such as undesired polymer diffusion. This approach is expected to be compatible with a wide variety of liquid-phase soluble initiators and precursor inks, facilitating room-temperature (RT) multi-materials 4D printing of hydrogels for wireless remote sensing and real-time monitoring of biological activities.

2. Experimental section

2.1. Materials

Titanium powder (99.5 %), aluminum powder (99.5 %), graphite (99 %), acrylamide (AM, AR), hydroxypropylmethyl cellulose (HPMC, 15000 mPa.s), *N*, *N*′-methylene diacrylamide (MBAA, 99 %), ammonium persulphate (APS, 98 %, Adamas), sodium chloride (NaCl AR).

2.2. Synthesis of the Ti_3AlC_2 MAX phase

Graphite, titanium powder, and aluminum powder were blended in a molar ratio of 1.8:3:2.2 and subjected to ball milling for 18 h. The resulting mixture was then heated to 1600 °C and held at this temperature for 8 h in an argon environment. Once cooled naturally, the sintered block was pulverised and passed through a 400-mesh sieve to yield particles smaller than 38 μm. The powder was subsequently treated with 9 M hydrochloric acid at 40 °C under continuous stirring for 72 h to eliminate intermetallic impurities. Following this, the powder was exhaustively washed with deionised water and dried under vacuum at 80 °C for 6 h. The final MAX-phase powder was stored in a glovebox for subsequent applications.

2.3. Wet-etching of the $Ti_3C_2T_x$ MXene

A quantity of 1 g of Ti_3AlC_2-MAX powder was gradually introduced into 20 ml of a mixed solution comprising concentrated HF (49 wt%), concentrated HCl (36 wt%), and DI-water in a volume ratio of 1:6:3. The MAX phase underwent etching at 35 °C for 48 h. Subsequently, the MXene product was purified via repeated centrifugation cycles using DI-water until a neutral pH of approximately 7 was attained.

2.4. Delamination of $Ti_3C_2T_x$ MXene

To facilitate the intercalation of Li^+ ions between MXene layers, multilayered MXene was agitated in a 20 mg/ml LiCl solution at 35 °C with a stirring speed of 300 rpm for 18 h. The LiCl was then eliminated through a series of centrifugation steps at 3500 rpm for 10 min, with the supernatant being discarded and the sediment redispersed in DI-water eight times. For the isolation of single-layer $Ti_3C_2T_x$ nanosheets, the centrifuged MXene sediment was redispersed in DI-water and subjected to vigorous shaking for 30 min using a vortex mixer. The resulting suspension was centrifuged at 3500 rpm for 1 h to yield an upper dispersion containing few-layered MXene, which was subsequently centrifuged at 12000 rpm for 1 h. The MXene slurry obtained from the bottom of the centrifuge tube was homogenised with a Mayer rod, and a few drops of water were added to adjust the MXene ink to the desired concentration. To determine the solid content C of the prepared MXene ink, a sample of M grams was vacuum-dried at 80 °C for 12 h, with the resulting dried powder weighing m grams. By repeating this procedure ten times, the solid content C was calculated using the formula $C = m/M$.

2.5. Characterization

The structure of MAX was confirmed by X-ray diffraction (XRD, Cu Kα radiation, λ = 1.54178 Å, D/max 2550 V, Rigaku) and the morphology was studied by scanning electron microscopy (SEM, ZEISS Sigma 300), transmission electron microscopy (TEM, Japan-JEOL-JEM 2100Plus), atomic force microscopy (AFM, Bruker Dimension Icon) and the elemental composition was characterized by Energy Dispersive Spectroscopy (EDS, OXFORD X-act one) and X-ray Photoelectron Spectroscopy (XPS, Thermo Scientific ESCALAB Xi+), Electron paramagnetic resonance (EPR, Bruker-EMXplus) spectroscopy was employed to detect the sulfate radicals produced. 5,5-dimethyl-1-pyrroline-N-oxide (DMPO) was used as the trapping agent for the radicals generated from the dissociation of APS by MXene. Fourier Transform infrared

spectroscopy (FTIR) were recorded using a FTIR spectrometer (SHIMADZU-IRTracer-100).

2.6. 4D printing

Ink preparation: The extrusion printing ink comprises acrylamide (monomer), MBAA (crosslinking agent), hydroxypropyl methylcellulose or HPMC (rheological modifier), and MXene slurry (trigger, ~50 mg/ml). Here, W denotes the monomer-to-water mass ratio, while C represents the crosslinking agent-to-monomer molar ratio. Initially, the monomer, water, and MXene slurry (W = 4:3) are combined and homogenised in a mortar grinder at 1500 rpm for 30 min. MBAA ($C = 1 \times 10^{-5}$) and HPMC (rheological modifier-to-water mass ratio = 1:16.7) are then introduced and mixed for 60 min to achieve a homogeneous, extrudable ink.

Preparation of the initiator solution: APS and water were blended in a 1:16 mass ratio, followed by 30 min of stirring, yielding the initiator solution.

Printing: A programmable three-axis pneumatic robotic deposition system (SM500ΩX-3ASS, MUSASHE), integrated with drafting software (MuCAD, MUSASHI), was employed to extrude-print highly elastic hydrogels. The process was conducted under consistent parameters: air pressure (30–60 kPa), nozzle speed (8–12 mm s^{-1}), and nozzle-to-base distance (350–450 μm). The prepared ink was dispensed through a cylindrical nozzle (14 G) into an initiator solution for mechanical testing. The pattern used for mechanical testing is printed in a snake like pattern to create a rectangular pattern (2 cm * 5 cm). For the subsequent printing of the strain sensor hydrogel and patterned structure, under the same conditions, we use a 21 G needle to print. For the finely arranged hydrogel structure printed in the article for optical microscope observation, the 30 G needle tube is used for printing.

Post-printing, the hydrogel was extracted from the initiator solution following a 30-min dwell period. To eliminate surface residual APS and enhance ionic conductivity, the printed hydrogel was washed for 10 min with a sodium chloride aqueous solution (0.2 g/ml). It was then left to equilibrate at room temperature for 30 min prior to further testing.

2.7. Rheological characterization

Rheological properties were conducted on a rotational rheometer (MCR302, Anton Paar GmbH, Austria). All steady-state shear and dynamic rheological tests were performed at room temperature using a 20 mm stainless steel parallel plate. Dynamic stress sweeps were carried out at a constant angular frequency of 1 rad·s^{-1}. Within the linear viscoelastic range of each sample, a series of oscillatory frequency sweep measurements were conducted.

2.8. Tensile testing

Uniaxial tensile testing was performed on 3D-printed dog-bone specimens at a constant strain rate of 100 mm/min via an electronic tensile tester. To mitigate grip slippage or shoulder distortion, the ends of the printed strips were affixed with abrasive paper, guaranteeing no slippage during testing and ensuring all samples fractured within their linear elastic regime. Stress was computed as the ratio of measured force to the original cross-sectional area, whereas strain was derived from displacement relative to the initial gauge length. The Young's modulus was obtained from the linear segment of the stress-strain curve.

2.9. Conductivity measurements

The resistance (Ω) of the hydrogel was measured using a VICTOR 4090C system. The relative resistance change was calculated by the following equation:

$$\frac{\Delta R}{R_0} = \frac{R_r - R_0}{R_0} \times 100\%$$

where R_r denotes the real - time resistance of the hydrogel during the deformation process, and R_0 denotes the resistance of the hydrogel in the initial state. The gauge factor (GF) was defined as:

$$GF = \left(\frac{\Delta R}{R_0}\right) \Big/ \varepsilon$$

where ε represents the applied strain.

The electrochemical impedance spectroscopy (EIS) curves were measured using a CHI760E electrochemical workstation, within a frequency range from 10^{-2} Hz to 10^{6} Hz. The ionic conductivity (σ) of the hydrogel electrolyte was computed in accordance with the following equation:

$$\sigma = \frac{l}{R \times A}$$

L and A represent the thickness and the test area of the hydrogel electrolyte respectively, and R is the ohmic resistance derived from the high - frequency intercept of the semi - circle in the Nyquist plot.

2.10. Measurement of water content

The Swelling degree (SD) of the hydrogel is determined by comparing the weights of the samples at equilibrium. It is calculated using the following equation:

$$SD = \frac{m - m_0}{m_0} \times 100\%$$

Herein, m represents the real - time weight of the hydrogel at various swelling times, while m_0 denotes the weight of the original hydrogel prior to swelling.

2.11. Application of epidermal strain sensors

Subtle electrophysiological signals are acquired via encapsulated hydrogel electrodes and commercial copper electrodes. Human movements and sound signals are detected by adhering hydrogel to the human body, and current signals are recorded in real time using an CHI760E electrochemical workstation. All participants signed the informed written consent prior to the research.

2.12. Construction of the wireless signal acquisition device

A strain sensor was integrated into a voltage divider circuit, comprising a 100 kΩ series resistor with a 5 V applied voltage. Voltage signals of the five sensors were individually sampled through five analog-to-digital converter (ADC) pins on an Arduino Nano. Data transmission was facilitated via a Bluetooth module. The entire wireless device was powered by two 18,650 batteries connected in series.

2.13. Machine learning framework

During the training phase, gesture signals from five channels were acquired using a smart glove. Active segments and rest segments were differentiated based on voltage ranges. The average voltage within each active segment was computed to generate a five-element array. A pretrained Residual Neural Network (ResNet), consisting of 32 convolutional layers and one fully connected layer, served as the starting point for transfer learning. Within the training model, feature vectors underwent dimensionality reduction through iterative processing across convolutional layers, followed by pooling layers and activation layers. Each gesture was repeated twenty times per participant to construct the training dataset. The parameters of model were adjusted to achieve

appropriate convergence. During the operational phase, all channel signals were continuously recorded, processed, and fed into the trained model. Corresponding gestures were dynamically recognized and translated into motion commands. These commands were wirelessly transmitted via Bluetooth to control a toy car equipped with an Arduino Uno microcontroller.

3. Results and discussion

3.1. MXene-triggered AIDP process

We start by describing the MXene synthesis. Ti_3AlC_2 MAX phase was sintered according to literature using titanium powder, graphite as Ti source, carbon source, respectively [32–34]. All XRD peaks are well indexed with the standard PDF card, together with the ternary layered morphology in the SEM image (Fig. S1), suggesting that the as-synthesized MAX phase (grain size ~25 μm) is of high-quality. Wet-etching of Ti_3AlC_2 results in accordion-like multilayered MXene (Fig. S2), which delaminates into MXene flakes with distinctly defined edges and a smooth surface upon manual shaking, as evidenced by the TEM (Fig. S3a). These flakes are ultrathin, as confirmed by the TEM and AFM (Fig. S3b).

Conventional hydrogel synthesis typically requires high-energy input, long polymerization time and/or high initiator (i.e., APS) concentration, yielding hydrogels with mediocre mechanical properties and large hysteresis. Very recently, we demonstrated the unique yet general MXene triggering chemistry that allows the rapid production of hydrogels at RT [30]. This fits exactly well with the 4D printing of hydrogels, as one needs to ensure the rapid solidification of the extruded filaments (at least on the top surface). As such, we propose the AIDP-assisted, high-precision 4D printing of robust hydrogels with highly entangled architectures enabled by the MXene triggering chemistry.

As schematically illustrated in Fig. 1a, the formulated inks are comprised of AM monomers, HPMC as thickener, MBAA as crosslinker and MXene flakes as the trigger. The high-molecular-weight HPMC renders pronounced steric hindrance in the ink, significantly retarding the free-flow of the filaments once 3D extruding into the dilute initiator solution. The initiator further diffuses into the extruded filaments where MXene further accelerates the production of free radials ($\cdot SO_4^-$). These radicals initiate time-resolved in-situ polymerization of AM monomer inside the filaments, yielding long-chain polymers that evolve into a chemically crosslinked, highly entangled hydrogel network. This dynamic polymerization mechanism facilitates the formation of hydrogel microstructures with exceptional elasticity and mechanical robustness. This AIDP-assisted strategy offers a versatile, RT-compatible platform for 4D printing of complex hydrogels, broadly applicable to systems

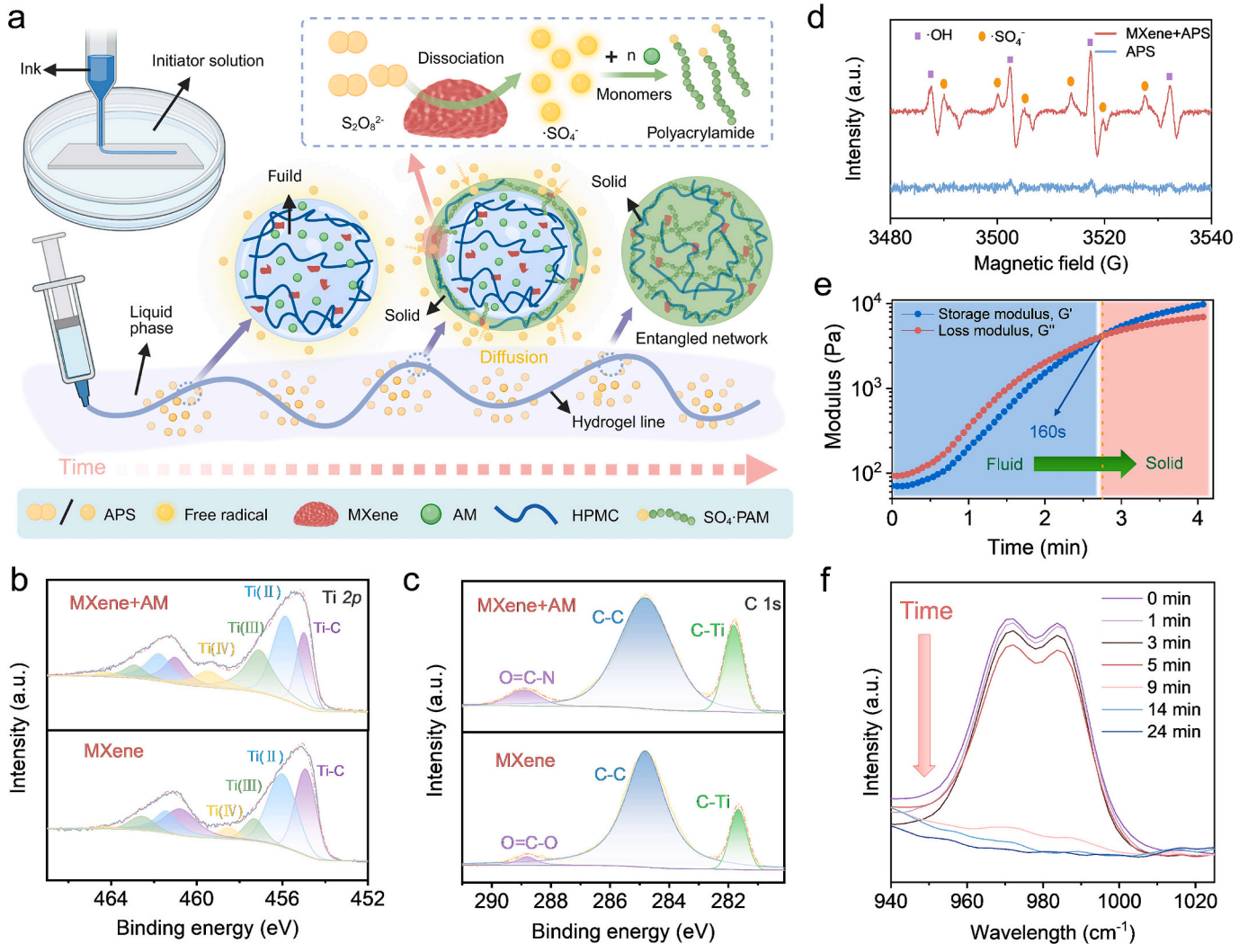

Fig. 1. 4D printing of hydrogels enabled by the MXene triggering chemistry. a) Schematic diagram of AIDP hydrogel process b) Ti 2p and c) C 1 s XPS spectra of MXene-AM powders. d) EPR spectra of MXene-APS solutions. e) The real-time evolution of storage (G') and loss modulus (G") of the precursor solutions. f) FTIR spectra change of the precursor solutions reacting with APS solutions at RT.

utilizing aqueous initiators and MXene-mediated radical triggers. It significantly expands the printable material library in DIW and introduces new avenues for constructing chemically tunable, mechanically resilient soft matter systems.

To elucidate the underlying mechanism of MXene-triggered AIDP, we conduct a series of spectroscopic and rheological analyses. As shown in the Ti $2p_{3/2}$ XPS spectra (Fig. 1b), pristine $Ti_3C_2T_x$ MXene exhibits characteristic peaks at 455.0, 456.0, 457.3, and 458.45 eV, corresponding to Ti—C, Ti(II), Ti(III), and Ti(IV), respectively [25]. Upon introduction of acrylamide (AM), the relative intensity of the Ti—C and Ti(II) peaks significantly decreases, while Ti(III) and Ti(IV) signals are notably enhanced (Table S1). The shift toward higher binding energies suggests the interfacial electronic delocalization from MXene to AM, indicative of coordination interactions between the electron-rich MXene surface and AM monomers. The C—Ti bond peak shifts from 281.8 eV (pristine MXene) to 281.6 eV in the MXene–AM system (Fig. 1c and Table S2), further supporting the occurrence of charge transfer at the interface.

EPR spectroscopy provides direct evidence for the MXene triggering effect (Fig. 1d). While aqueous APS alone shows negligible radical signals under ambient conditions, the addition of MXene instantly produces strong signals corresponding to sulfate and hydroxyl radicals. This observation aligns well with our reported mechanism, which MXene triggers the APS decompostion to $\cdot SO_4^-$, the key to the accelerated AM polymerization at RT [30]. This is further confirmed by the modulus analysis. Upon contacting the APS solution, the storage modulus (G') and loss modulus (G") of the precursor ink rapidly increase within tens of seconds, confirming fast gelation triggered by MXene-mediated radical generation (Fig. 1e). The ink remains the viscoelastic fluid within 165 s (as G" > G'), beyond which phase change occurs from fluid to elastic solid (as G' > G“), indicative of solidification completion (at least on the ink surface). In contrast, the G' and G" shows little variation in the inks without MXene (Fig. S4). It's worth noting that our minutes-scale solidification time is much shorter compared to the rest of hydrogels' gelling time, suggesting the potentially scalable production of large hydrogels is cost-effective.

Over time, the sulfate radicals triggered by MXene flakes induce the generation of short-chain monomer radicals, which progressively propagate to form long-chain polymers. Due to the initiator (aq.) concentration is low, this time-dependent polymer growth gradually forms highly entangled network structure within the printed filaments [35]. FTIR was employed to track the time-resolved monomer conversion [23] (Fig. 1f). Upon exposure to APS at RT, the intensity of the acrylamide C═C stretching peak in the ink decreases steadily. After ~9 min, the conversion of C═C double bonds reaches ~88.8 %, with ongoing polymerization observed thereafter (Fig. S5).

Collectively, both modulus and FTIR data confirm the plausibility of AIDP-assisted 4D printing enabled by MXene triggering chemistry. This allows rapid structural fixation of 3D-printed hydrogel filaments within a short timescale, followed by sustained chain propagation and network entanglement during post-curing with time. As such, our strategy is expected to achieve high-precision, rapid printing of resilient hydrogels with long-chain, entangled hydrogel networks, as will be discussed below.

3.2. Demonstration of AIDP-assisted 4D printing

Next, we demonstrate the AIDP-assisted 4D printing. The ink exhibits a shear-thinning, non-Newtonian behavior (Fig. 2a) with a thixotropy phenomenon (Fig. 2b). By applying a yield stress over 90 Pa, the ink G" dominates G', suggesting that the ink becomes flowable, allowing for continuous extrusion through the nozzle (Fig. 2c). Upon the removal of applied stress, the G' surpasses G", indicating that the shape of as-extruded lines can be well preserved with minimal swelling (Fig. S6 and Video S1). Therefore, a variety of texts (such as MXene Sichuan university) and stretchable patterns (Fig. 2d and Video S3) as well as compressible cones arrays and 3D rectangular block (Fig. 2e, Fig. S7 and Video S4) are successfully printed, highlighting the broad applicability of our printing technique in producing stretchable, compressible hydrogel-based electronic skins. To reveal the printing accuracy, hydrogel lines were 4D-printed and imaged using the optical microscopy (Fig. 2f). The extruded hydrogel filaments tend to form trapezoidal or dome-like geometries (Fig. S8), a prerequisite of high-resolution printing. These printed lines are uniform and straight with a line width of 162 μm and line spacing of 51 μm, respectively (Fig. 2g). The variation of line width is as low as 0.53 % while the gap variation is slightly higher (1.86 %, Fig. 2h). The high spatial uniformity in the rapid-printed structures indicate that our AIDP-assisted 4D printing holds a bright future in hydrogel-based electronic skins.

3.3. Analysis of highly entangled hydrogel networks

Recent work by Suo and co-workers demonstrated that under conditions of high monomer content and low crosslinker concentration, sparse chemical crosslinking induces dense chain entanglement [32]. Notably, such hydrogels retain low hysteresis, low friction, and high wear resistance even after reaching swelling equilibrium in water. To this end, we formulated precursor inks with a molar ratio of MBAA crosslinker to AM monomer (54.8 wt%) of 10^{-5}:1, and 4D printed polyacrylamide (PAM) hydrogels with highly entangled chains network at RT. The tensile stress–strain profiles of printed hydrogels strips vary profoundly with MXene content (Fig. 3a). The hydrogel printed with 0.64 wt‰ MXene exhibits the highest Young's modulus (126 kPa), tensile strength (743 kPa), and fracture strain (~600 %). Insufficient MXene leads to less radicals to fully proceed polymerization, resulting in inferior mechanical strength compared to those triggered by a higher MXene content.

We further analyze the hysteresis behavior of as-printed hydrogel strips to evaluate the entanglement density of these networks. As shown in Fig. 3b, c, hydrogels with a low MXene content exhibit a hysteresis ratio of ~26 % at 200 % strain, indicative of loose network structures and poor stress dissipation due to low polymerization density. Nevertheless, too much MXene content initiate excessive physical crosslinking and leads to increased hysteresis (Fig. S9). A lowest hysteresis ratio below 6 % is achieved in the hydrogel with 0.64 wt‰ MXene, suggesting the formation of highly elastic hydrogel networks at this optimal MXene content. Indeed, indivdual 4D-printed hydrogel stips also exhibit similar high modulus and low hysteresis as the bulk hydrogel (Fig. S10), which can be well maintained over 1000 cycles of large-deformation loading (Fig. 3d). Unlike traditional polymer hydrogels, the tensile response of 4D printed hydrogels is almost independent of the stretching rate. Within the strain rate range of 20–200 mm/min, the optimized 4D-printed hydrogel exhibits a hysteresis ratio of 2.93 % at 200 % strain, demonstrating its excellent elasticity (Fig. S11).

Since the storage modulus (G') in the high-frequency region can be used to indicate the state of crosslinking and entanglement inside the hydrogel [36]. we employed the rheological measurements to unveil the advantage of entangled network in MXene-triggered 4D-printed hydrogel over thermally polymerized networks in conventional hydrogels. As shown in Fig. 3e, the G' of the MXene-triggered 4D-printed hydrogel is approximately twice that of the conventional hydrogel. Since the monomer-to-crosslinker molar ratio and the swelling mass fraction are same in both hydrogels, the number of covalent crosslinking points is deemed as similar, it thus can be fairly assumed that MXene-triggered 4D-printed hydrogel has a higher number of chains entanglements than the thermally initiated hydrogel.

Fig. 3f compares the swelling of MXene-triggered 4D-printed hydrogel with conventionally thermal-initiated hydrogel, showing a three times lower swelling than that of thermal-initiated hydrogel after immersing in water for 720 min (Fig. S12). This also demonstrates that MXene-triggered monomer crosslinking induces a greater number of entanglement structures [37]. The exceptional strength, together with

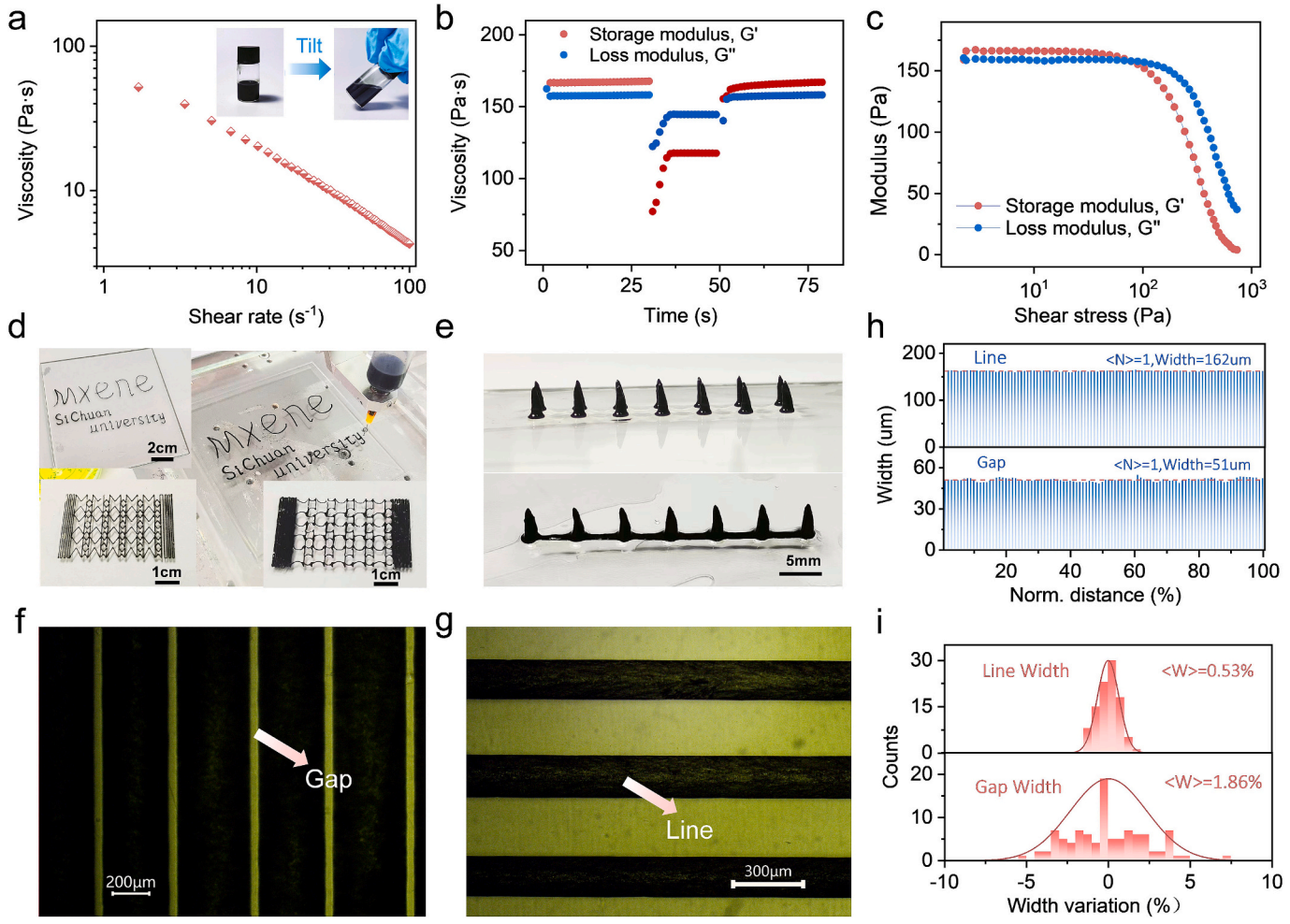

Fig. 2. High precision hydrogel 4D printing. Rheological properties of the precursor inks with viscosity plotted as a function of a) shear rate and b) interval shearing time. c) Storage modulus (G') and loss modulus (G") of the precursor inks versus shear stress. d) The real-time AIDP-assisted 4D printing of "MXene SiChuan University" (After forming in the initiator solution, remove it), as well as optical images of high-resolution of 4D-printed stretchable structures. e) AIDP-assisted 4D printing of hyrogel-based cones-like arrays (After forming in the initiator solution, remove it). Print optical images of f) gap and g) line of periodic hydrogels. h) Gap width and line width distribution and i) their variation of AIDP-assisted 4D-printed hydrogel lines.

the minimal hysteresis and electrical property in our MXene-triggered, 4D-printed hydrogel outperforms the rest of hydrogels known in terms of these key parameters (Fig. 3g and Table S3). For instance, polyvinyl alcohol (PVA) freeze-thaw hydrogels—known for their crystalline domains—deliver high tensile strength at the cost of compromised elasticity, while cast hydrogels exhibit low energy dissipation (hysteresis) with unsatisfied mechanical strength.

3.4. *Sensing performance of 4D printed elastic hydrogel*

We 4D-printed a single line of hydrogel and conducted corresponding electrical performance tests. The single line exhibits a high stretchability (~600 %) and sensitivity over a large linear range (GF = 5.5), among other properties (Fig. S13a). We note that a sensitivity of 5.5 has not been reported over such a wide stretchablity range yet, suggesting the broad potential application of our 4D printed hydrogel for multiple scenarios sensing. EIS was used to evaluate the ionic conductivity of hydrogel lines printed with different MXene contents (Fig. 4a, Fig. S13b). The ionic conductivity decreases as increasing the MXene content, which can be fairly attributed to the denser crosslinked structure enabled by the high MXene content, leading to sluggish ion migration. The encapsulated strain sensor based on 4D-printed hydrogel (Fig. 4b) exhibits an excellent elasticity with a low hysteresis, likely due to the highly entangled network structure of the hydrogel (Fig. 4c). To evaluate the stability of the sensor's electrical signal under different stretching frequencies, repeated stretches were applied at varying frequencies (0.1, 0.2, 0.5, and 1 Hz). The strain sensor demonstrates stable electrical signals under different frequencies (0.1–1 Hz, Fig. 4d), stretching magnitudes (10–90 %, Fig. 4e, f) or voltages (0–200 % strain, Fig. 4g), indicative of remarkably stable sensitivity in the 4D-printed hydrogel. The strain sensor responses within 3 s upon applying 50 % strain, guaranteeing potential swift detection without severe signal delaying (Fig. S14). Even after ~750 loading-unloading cycles at 100 % strain, the strain sensor showcases no obvious signal drift or fluctuation, confirming its high mechanical durability and long-term cyclic stability (Fig. 4h). Moreover, the abundant hydrogen bonds in the network endows the self-healing property in the 4D-printed hydrogel. As shown in Fig. S15a, the 4D-printed MXene hydrogel strip is able to conduct direct-current electricity to light up a bulb. After cutting the hydrogel, the bulb turns off, and by simply rejoining two cut strips, the bulb lights up again after 1.6 s (Fig. S15b). The self-healed hydrogel shows negligible initial conductivity drift after rejoining and maintains consistent electrical properties even under 25 % strain (Fig. S13c).

Moreover, the 4D-printed hydrogel-based strain sensor—featuring superior ionic conductivity, high elasticity, and minimal hysteresis—enables precise monitoring of subtle electrophysiological signals (i.e., muscle activity, vocal patterns, and carotid artery signals in sports rehabilitation). For instance, when the strain sensor is placed on the

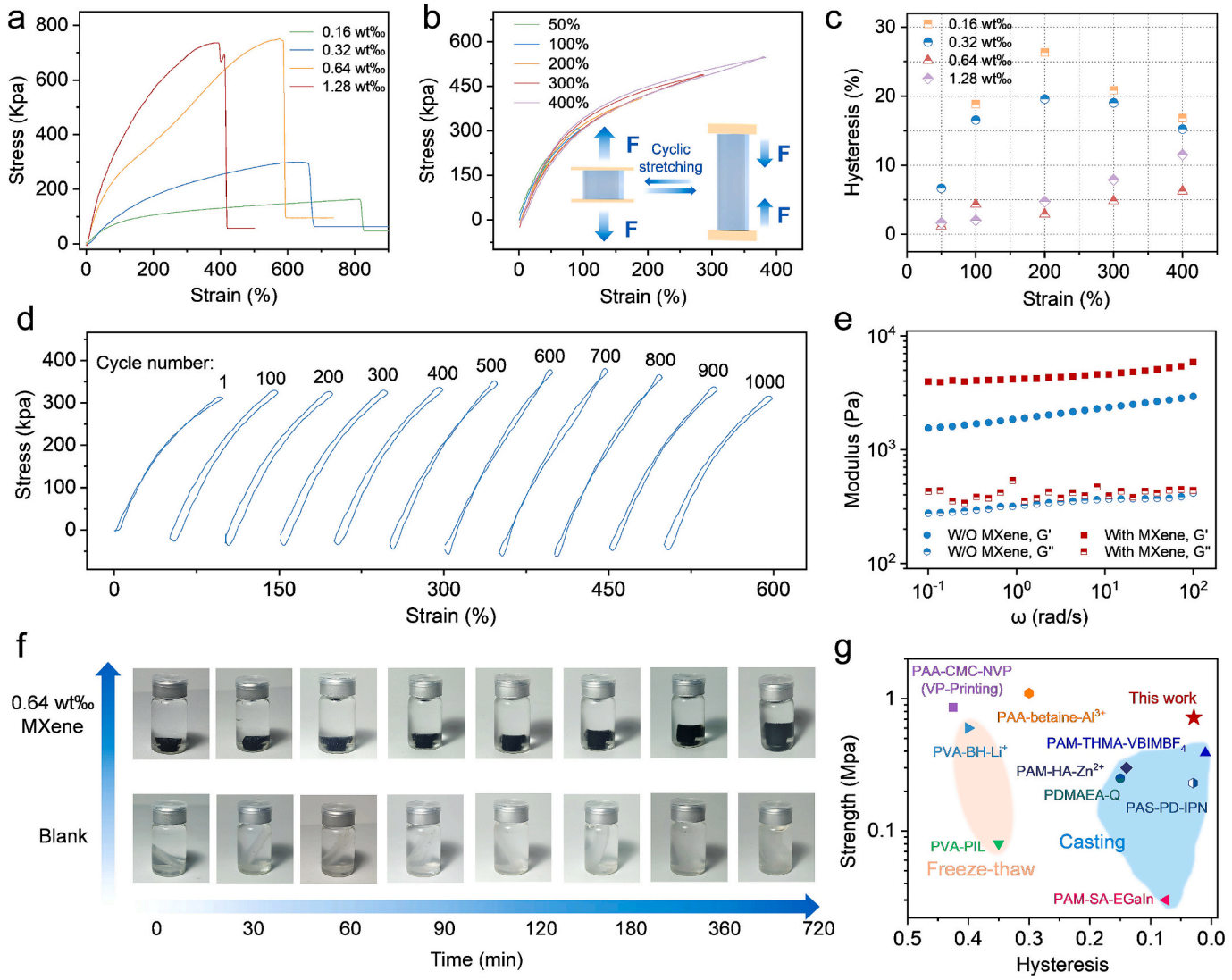

Fig. 3. Mechanical properties of highly entangled hydrogels. a) Tensile stress-strain curves of hydrogels with different MXene contents at 100 mm/min. b) Loading-unloading tensile curves of hydrogels at strains ranging from 50 to 400 % at a deformation rate of 100 mm/min. c) Hysteresis of hydrogels at each strain cycle under different strain rates. d) Stress-strain curves of MXene-triggered 4D-printed hydrogel over 1000 loading-unloading cycles at a 100 % strain. The curves are horizontally offset for clarity. The cycling numbers are shown on the curves. Comparison one) modulus and f) Anti-swelling properties of MXene-triggered 4D-printed hydrogels with thermal-initiated hydrogel. g) Mechanical strength and hysteresis ratio comparison of MXene-triggered 4D-printed hydrogels with reported hydrogels with similar strength [38–46].

larynx during speech (hydrogel, MXene), it captures well-defined signal peaks with high repeatability (Fig. 5a, Fig. S16), suggesting the promising applications for voice-based diagnosis of disorders like Parkinson's disease and PTSD. The strain sensor can be used for pulse detection, best evidenced by the monitoring of three primary waveforms (percussion-, tidal-, dicrotic-) in the recorded carotid pulse in Fig. 5b. Similarly, the 4D-printed hydrogel-based strain sensor is capable of monitoring the handwriting (Fig. 5c) and finger movements (Fig. S17), showing consistent, posture-dependent signal patterns with great reproducibility. These findings highlight the strain sensor's versatility in post-surgical rehabilitation and its promising applications in tracking cardiovascular and neurological health.

Advancing further, we embed 4D-printed hydrogel-based strain sensors into a multifunctional smart glove for wirelessly car controlling (Fig. S18a). As shown in Fig. 5d, the entire system comprises finger-joints-activity signal capture, data processing, wireless transmission, and smart car motion control. The captured signals are translated into sign language gesture recognition, and fused with state-of-the-art machine learning algorithms, enabling wireless remote control of a car with multi-degree freedom. For signal-driven sign language gesture recognition and translation, a convolutional neural network (CNN) machine learning algorithm classifies and identifies signals from distinct gestures (Fig. 5e). Fig. 5f displays signals from six gestures, demonstrating consistent repeatability across repeated motions.

The dataset was then split into two overlapping subsets: 80 % for training and 20 % for testing. Fig. S18b employs a confusion matrix to evaluate the machine learning model, which attains robust classification accuracy and stability after 100 training epochs. Live demonstrations, captured in Video S2 and images, show real-time wireless car control via a volunteer's armband equipped with 4D-printed hydrogel strain sensors (Fig. 5g). This showcases the versatility of our highly entangled, ion-conductive 4D-printed hydrogels for next-generation human-machine interfaces and flexible electronics.

4. Conclusion

In summary, we have developed a novel AIDP-assisted 4D printing of highly entangled hydrogels enabled by the unique MXene triggering

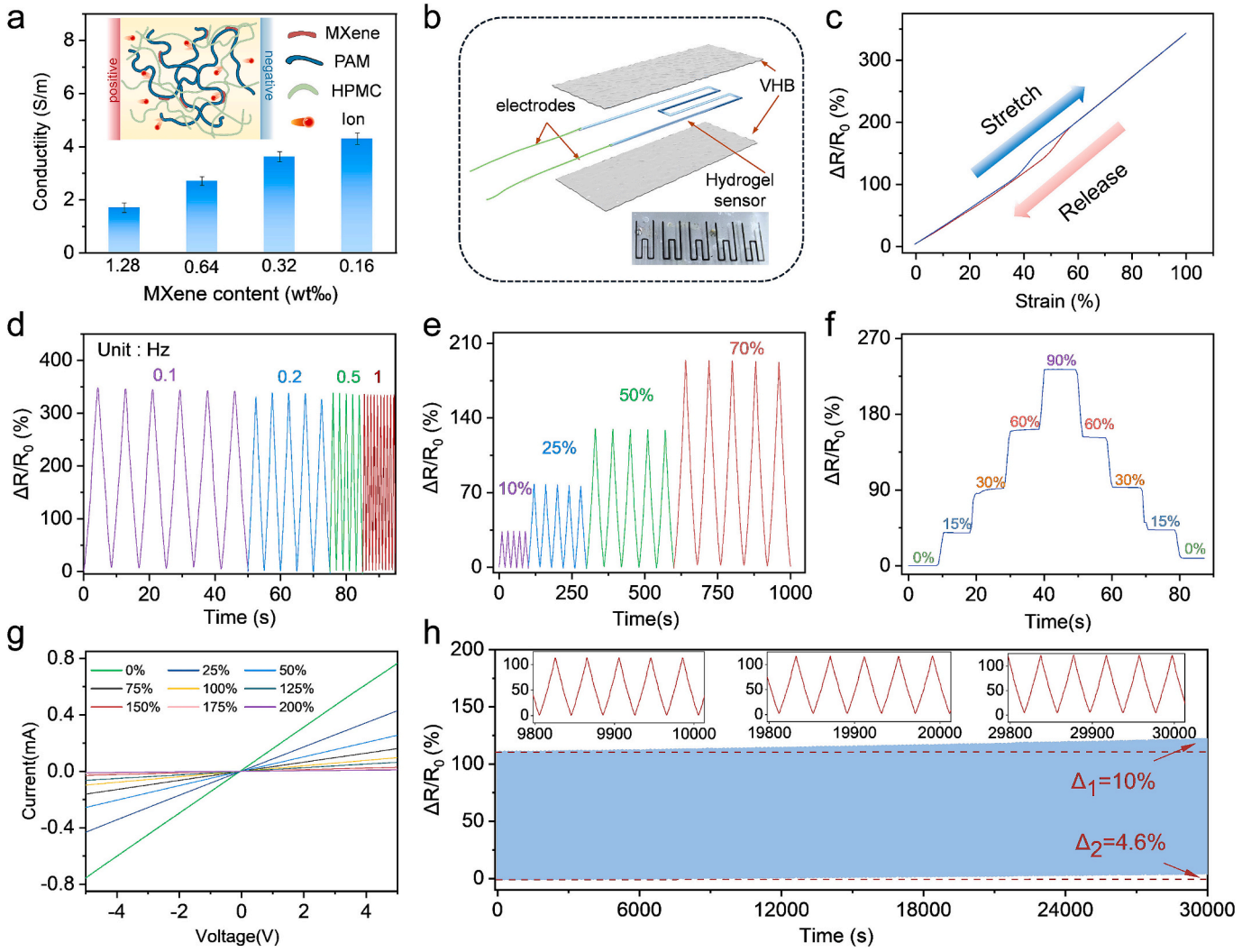

Fig. 4. Electrical properties of MXene triggered 4D printed hydrogel. a) Effect of different MXene solid content on the ionic conductivity of 4D-printed hydrogel. b) Schematic illustration of an encapsulated strain sensor, inset is an optical image of printed hydrogel. c) Loading-unloading resistance curves of MXene hydrogels under 100 % strain. Five cycle cyclic resistance curves of MXene hydrogel at d) different tensile frequencies and e) different strains. f) Resistance change rate of MXene hydrogel during rapid, consecutive stretching at various strains. g) Scanning curves of MXene hydrogels with different strain degrees in a wide voltage range (-5 V–5 V). h) Long-term cyclic sensing stability of MXene hydrogel under 50 % strain.

chemistry. This approach overcomes critical limitations in conventional hydrogel printing—such as poor shape fidelity, uncontrolled polymerization, and unstable networks—by leveraging: (a) MXene rapidly generates sulfate radicals upon contact with aqueous APS, enabling instantaneous interfacial polymerization to lock extruded geometries (achieving high-fidelity 162 μm line resolution). (b) Time-dependent network evolution: Subsequent slow polymerization in a low-crosslinker/high-monomer environment constructs dense, highly entangled networks, endowing hydrogels with exceptional elasticity, ultra-low hysteresis (~2.93 %). The 4D-printed hydrogels exhibit outstanding ionotronic properties, including high ionic conductivity, strain-sensitive resistance, and self-healing behavior. These wearable strain sensors enable high-fidelity monitoring of physiological signals (e.g., laryngeal movement, carotid pulse) and construction of robust, controllable, real-time human-machine interfaces with >98 % gesture recognition accuracy. However, it is worth noting that the AIDP technique described in this work relies on a diffusion-initiated polymerization process triggered by the initiator, which has been verified in our experiments. Meanwhile, the monomers also tend to diffuse outward through the hydrogel matrix, potentially leading to a radial gradient within the network structure and a gradual decrease in monomer concentration. This outward diffusion may further induce epitaxial growth of monomers on the hydrogel surface. These issues will be systematically investigated in our future studies, with particular focus on the growth behavior of the hydrogel network and the additional functionalities that may be induced by such diffusion-mediated processes. Overall, this work establishes AIDP as a generalizable platform for fabricating structurally complex, functionally adaptive hydrogels, opening avenues for advanced bioelectronics, soft robotics, and personalized healthcare devices.

Supplementary data to this article can be found online at https://doi.org/10.1016/j.cej.2025.170043.

CRediT authorship contribution statement

Qinglong He: Writing – original draft, Methodology, Investigation, Formal analysis, Data curation, Conceptualization. **Chendong Zhao:** Writing – review & editing, Methodology, Investigation, Formal analysis, Data curation, Conceptualization. **Yuanjie Jiang:** Investigation, Formal analysis. **Jimei Liu:** Investigation. **Xinyu Liu:** Formal analysis. **Rui Jia:** Software. **Cheng Yang:** Software. **Mengzhou Liao:** Writing – review & editing, Methodology. **Yan Zhao:** Writing – review & editing,

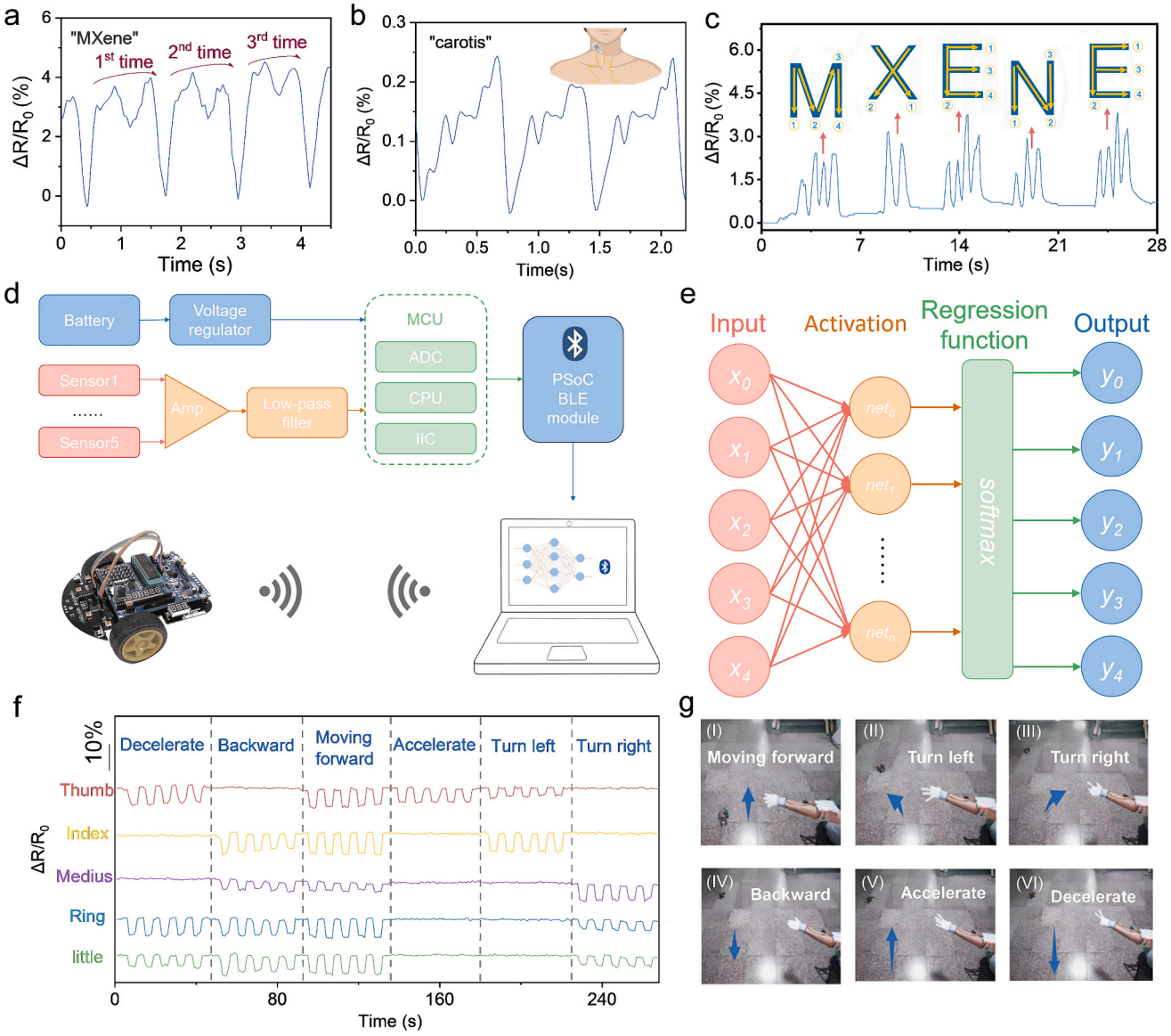

Fig. 5. Application of 4D-printed hydrogel-based strain sensor. Real-time monitoring of a) human voice, b) pulse, and c) handwritten signals, respectively. The inset shows the tensil sensor attached to the b) carotid artery. d) Schematic illustration of a synchronous intelligent wireless car control system on collected finger bending signals. e) The framework of a machine learning algorithm based on convolutional neural networks (CNNs) for sign language hand gesture recognition using collected finger bending signals. f) Electrical signals collected from the sensing performances to the different sign language gestures. g) The real-time control of the intelligent wireless car movement by the MXene hydrogel sensor-integrated armband attached on the arm of the volunteer: (I) the intelligent car starts and moves forward, (II) the intelligent car turns left, and (III) turns right, and (IV) the intelligent car backwards, and (V) the intelligent car accelerates and (VI) decelerates.

Formal analysis. **Desheng Kong:** Writing – review & editing, Methodology, Formal analysis. **Valeria Nicolosi:** Writing – review & editing. **Caofeng Pan:** Writing – review & editing, Methodology, Formal analysis. **Chuanfang Zhang:** Writing – review & editing, Supervision, Resources, Project administration, Funding acquisition, Formal analysis.

Declaration of competing interest

The authors declare that they have no known competing financial interests or personal relationships that could have appeared to influence the work reported in this paper.

Acknowledgements

This work is generously supported by the Fundamental Research Funds for the Central Universities (1082204112A26, 20826044D3083, 20822041G4080), Natural Science Foundation of China (Grant No. 22209118, 00301054A1073, 22479101) and Open research fund of State Key Laboratory of Mesoscience and Engineering (MESO-23-D06).

Data availability

Data will be made available on request.

References

[1] P. Lu, D. Ruan, M. Huang, M. Tian, K. Zhu, Z. Gan, Z. Xiao, Harnessing the potential of hydrogels for advanced therapeutic applications: current achievements and future directions, Sig Transduct Target Ther 9 (2024) 1–66, https://doi.org/10.1038/s41392-024-01852-x.

[2] J. Jiang, E. Daatselaar, H. Wijnja, T. Gans, M. Schellevis, C. Venner, D. Brilman, C. Visser, Scalable jet-based fabrication of PEI-hydrogel particles for CO_2 capture, Energy Environ. Mater. 7 (2025) e12748, https://doi.org/10.1002/eem2.12748.

[3] L. Qin, J. Jiang, L. Hou, F. Zhang, J. Rosen, Thick electrodes of a self-assembled MXene hydrogel composite for high-rate energy storage, Energy Environ. Mater. 7 (2025) e12653, https://doi.org/10.1002/eem2.12653.

[4] X. Hu, M. Vatankhah-Varnoosfaderani, J. Zhou, Q. Li, S.S. Sheiko, Weak hydrogen bonding enables hard, strong, tough, and elastic hydrogels, Adv. Mater. 27 (2015) 6899–6905, https://doi.org/10.1002/adma.201503724.
[5] Y. Choi, J. Kim, B. Kang, H. Kim, Perspectives on hydrogel-based ionic thermoelectrics: from mechanistic insights to wearable applications of thermo-diffusive ionic materials, Energy Mater. 5 (2025), 500106. https://doi.org/10.20517/energymater.2025.50.
[6] X. Zhao, X. Chen, H. Yuk, S. Lin, X. Liu, G. Parada, Soft materials by design: unconventional polymer networks give extreme properties, Chem. Rev. 121 (2021) 4309–4372, https://doi.org/10.1021/acs.chemrev.0c01088.
[7] Y. Wu, R. He, B. Tan, L. Li, J. Liao, An injectable hydrogel for chemodynamic therapy-induced ferroptosis in malignant melanoma, Chin. Chem. Lett. (2025) 111339, https://doi.org/10.1016/j.cclet.2025.111339.
[8] P. Zhao, M. Li, J. Wang, J. Li, Y. Lin, Targeting the immune microenvironment: a novel strategy for treating infected bone defects with hydrogels, Chin. Chem. Lett. (2025) 111319, https://doi.org/10.1016/j.cclet.2025.111319.
[9] Y. Wang, H. Zhang, Y. Zhao, M. Liu, M.-J. Yin, Q.-F. An, Y. Li, In-situ photopolymerization hydrogel bioadhesive for on-demand rapid sealing of kidney wounds, Chin. Chem. Lett. (2025) 111483, https://doi.org/10.1016/j.cclet.2025.111483.
[10] K. Yao, Y. Shen, C. Chen, F. Qin, S. Song, X. Dong, W. Liu, Physically and chemically crosslinked rare-earth-doped hydrogels with dual fluorescence/conductive sensing abilities, Chin. Chem. Lett. (2025) 111531, https://doi.org/10.1016/j.cclet.2025.111531.
[11] S. Duan, Q. Shi, J. Hong, D. Zhu, Y. Lin, Y. Li, W. Lei, C. Lee, J. Wu, Water-modulated biomimetic hyper-attribute-gel electronic skin for robotics and skin-attachable wearables, ACS Nano 17 (2023) 1355–1371, https://doi.org/10.1021/acsnano.2c09851.
[12] X. He, J. Shi, Y. Hao, M. He, J. Cai, X. Qin, L. Wang, J. Yu, Highly stretchable, durable, and breathable thermoelectric fabrics for human body energy harvesting and sensing, Carbon Energy 4 (2022) 621–632, https://doi.org/10.1002/cey2.186.
[13] C. Yang, Z. Suo, Hydrogel ionotronics, Nat. Rev. Mater. 3 (2018) 125–142, https://doi.org/10.1038/s41578-018-0018-7.
[14] S. Park, H. Yuk, R. Zhao, Y.S. Yim, E.W. Woldeghebriel, J. Kang, A. Canales, Y. Fink, G.B. Choi, X. Zhao, P. Anikeeva, Adaptive and multifunctional hydrogel hybrid probes for long-term sensing and modulation of neural activity, Nat. Commun. 12 (2021) 3435, https://doi.org/10.1038/s41467-021-23802-9.
[15] Z. Zhong, M. Quiñones-Pérez, Z. Dai, V.M. Juarez, E. Bhatia, C.R. Carlson, S. B. Shah, A. Patel, Z. Fang, T. Hu, M. Allam, S.L. Hicks, M. Gupta, S.L. Gupta, E. Weeks, S.D. Vagelos, A. Molina, A. Mulero-Russe, A. Mora-Boza, D.J. Joshi, R. P. Sekaly, T. Sulchek, S.L. Goudy, J. Wrammert, K. Roy, J.M. Boss, A.F. Coskun, C. D. Scharer, A.J. García, J.L. Koff, A. Singh, Human immune organoids to decode B cell response in healthy donors and patients with lymphoma, Nat. Mater. 24 (2025) 297–311, https://doi.org/10.1038/s41563-024-02037-1.
[16] Q. Guan, S. Hou, K. Wang, L. Li, Y. Cheng, M. Zheng, C. Liu, X. Zhao, J. Zhou, P. Li, X. Niu, L. Wang, Y. Fan, Micropore structure engineering of injectable granular hydrogels via controlled liquid-liquid phase separation facilitates regenerative wound healing in mice and pigs, Biomaterials 318 (2025) 123192, https://doi.org/10.1016/j.biomaterials.2025.123192.
[17] C. Cui, Z.-Y. Zhuang, H.-L. Gao, J. Pang, X.-F. Pan, S.-H. Yu, 3D printing of ultrahigh filler content composites enabled by granular hydrogels, Adv. Mater. n/a (n.d.) 2500782. doi:https://doi.org/10.1002/adma.202500782.
[18] A.P. Dhand, M.D. Davidson, J.A. Burdick, Lithography-based 3D printing of hydrogels, Nat Rev Bioeng 3 (2025) 108–125, https://doi.org/10.1038/s44222-024-00251-9.
[19] Y. Zhu, Q. Zhang, J. Ma, P. Das, L. Zhang, H. Liu, S. Wang, H. Li, Z.-S. Wu, Three-dimensional (3D)-printed MXene high-voltage aqueous micro-supercapacitors with ultrahigh areal energy density and low-temperature tolerance, Carbon Energy 6 (2024) e481, https://doi.org/10.1002/cey2.481.
[20] R. Levato, T. Jungst, R.G. Scheuring, T. Blunk, J. Groll, J. Malda, From shape to function: the next step in bioprinting, Adv. Mater. 32 (2020) 1906423, https://doi.org/10.1002/adma.201906423.
[21] A. Ding, F. Tang, E. Alsberg, 4D printing: a comprehensive review of technologies, materials, stimuli, design, and emerging applications, Chem. Rev. 125 (2025) 3663–3771, https://doi.org/10.1021/acs.chemrev.4c00070.
[22] M. Champeau, D.A. Heinze, T.N. Viana, E.R. de Souza, A.C. Chinellato, S. Titotto, 4D Printing of Hydrogels: A Review, Adv. Funct. Mater. 30 (2020) 1910606, https://doi.org/10.1002/adfm.201910606.
[23] A.P. Dhand, M.D. Davidson, H.M. Zlotnick, T.J. Kolibaba, J.P. Killgore, J. A. Burdick, Additive manufacturing of highly entangled polymer networks, Science 385 (2024) 566–572, https://doi.org/10.1126/science.adn6925.
[24] P. Fu, H. Li, J. Gong, Z. Fan, A.T. Smith, K. Shen, T.O. Khalfalla, H. Huang, X. Qian, J.R. McCutcheon, L. Sun, 4D printing of polymers: techniques, materials, and prospects, Prog. Polym. Sci. 126 (2022) 101506, https://doi.org/10.1016/j.progpolymsci.2022.101506.
[25] K. Li, J. Zhao, A. Zhussupbekova, C.E. Shuck, L. Hughes, Y. Dong, S. Barwich, S. Vaesen, I.V. Shvets, M. Möbius, W. Schmitt, Y. Gogotsi, V. Nicolosi, 4D printing of MXene hydrogels for high-efficiency pseudocapacitive energy storage, Nat. Commun. 13 (2022) 6884, https://doi.org/10.1038/s41467-022-34583-0.
[26] S.J. Wu, J. Wu, S.J. Kaser, H. Roh, R.D. Shiferaw, H. Yuk, X. Zhao, A 3D printable tissue adhesive, Nat. Commun. 15 (2024) 1215, https://doi.org/10.1038/s41467-024-45147-9.
[27] B. Cai, D. Kilian, D. Ramos Mejia, R.J. Rios, A. Ali, S.C. Heilshorn, Diffusion-based 3D bioprinting strategies, Adv. Sci. 11 (2024) 2306470, https://doi.org/10.1002/advs.202306470.
[28] A.X. Ding, O. Jeon, D. Cleveland, K.L. Gasvoda, D. Wells, S.J. Lee, E. Alsberg, Jammed micro-flake hydrogel for four-dimensional living cell bioprinting, Adv. Mater. 34 (2022) 2109394, https://doi.org/10.1002/adma.202109394.
[29] Y.B. Lee, Y.S. Kim, C. Chen, M. Hossain, B. Suslick, R. Ewoldt, S. Tawfick, J. Moore, N. Sottos, P. Braun, Multimaterial 3D printing in activating bath enables in situ polymerization of thermosets with intricate geometries and diverse elastic behaviors, Adv. Mater. (2025) e08568, https://doi.org/10.1002/adma.202508568.
[30] W. Zhang, C. Zeng, M. Zhang, C. Zhao, D. Chao, G. Zhou, C. Zhang, MXene triggered free radical polymerization in minutes toward all-printed Zn-ion hybrid capacitors and beyond, Angew. Chem. Int. Ed. 64 (2025) e202413728, https://doi.org/10.1002/anie.202413728.
[31] S. Abdolhosseinzadeh, X. Jiang, H. Zhang, J. Qiu, C. Zhang, Perspectives on solution processing of two-dimensional MXenes, Mater. Today 48 (2021) 214–240, https://doi.org/10.1016/j.mattod.2021.02.010.
[32] C.E. Shuck, M. Han, K. Maleski, K. Hantanasirisakul, S.J. Kim, J. Choi, W.E.B. Reil, Y. Gogotsi, Effect of Ti3AlC2 MAX phase on structure and properties of resultant Ti3C2Tx MXene, ACS Appl. Nano Mater. 2 (2019) 3368–3376, https://doi.org/10.1021/acsanm.9b00286.
[33] Y. Choi, J. Kim, B. Kang, H. Kim, Perspectives on hydrogel-based ionic thermoelectrics: from mechanistic insights to wearable applications of thermo-diffusive ionic materials, Energy Mater. 5 (2025), 500106. https://doi.org/10.20517/energymater.2025.50.
[34] Z. Cui, C. Li, W. Peng, J. Liu, Emerging MXene-based electrocatalysts for efficient nitrate reduction to ammonia: recent advance, challenges, and prospects, Energy Mater. 4 (2024), 400057. https://doi.org/10.20517/energymater.2023.134.
[35] J. Kim, G. Zhang, M. Shi, Z. Suo, Fracture, fatigue, and friction of polymers in which entanglements greatly outnumber cross-links, Science 374 (2021) 212–216, https://doi.org/10.1126/science.abg6320.
[36] G. Nian, J. Kim, X. Bao, Z. Suo, Making highly elastic and tough hydrogels from doughs, Adv. Mater. 34 (2022) 2206577, https://doi.org/10.1002/adma.202206577.
[37] P. Liu, Y. Zhang, Y. Guan, Y. Zhang, Peptide-crosslinked, highly entangled hydrogels with excellent mechanical properties but ultra-low solid content, Adv. Mater. 35 (2023) 2210021, https://doi.org/10.1002/adma.202210021.
[38] X. Liu, X. Ji, R. Zhu, J. Gu, J. Liang, A microphase-separated design toward an all-round ionic hydrogel with discriminable and anti-disturbance multisensory functions, Adv. Mater. 36 (2024) 2309508, https://doi.org/10.1002/adma.202309508.
[39] Y. Wu, Y. Zeng, Y. Chen, C. Li, R. Qiu, W. Liu, Photocurable 3D printing of high toughness and self-healing hydrogels for customized wearable flexible sensors, Adv. Funct. Mater. 31 (2021) 2107202, https://doi.org/10.1002/adfm.202107202.
[40] S. Guan, C. Xu, X. Dong, M. Qi, A highly tough, fatigue-resistant, low hysteresis hybrid hydrogel with a hierarchical cross-linked structure for wearable strain sensors, J Mater Chem A 11 (2023) 15404–15415, https://doi.org/10.1039/D3TA02584E.
[41] W. Zhao, H. Zhou, W. Li, M. Chen, M. Zhou, L. Zhao, An environment-tolerant ion-conducting double-network composite hydrogel for high-performance flexible electronic devices, Nano-Micro Lett. 16 (2024) 99, https://doi.org/10.1007/s40820-023-01311-2.
[42] Q. Yang, W. Yang, Z. Wang, R. Chen, M. Li, C. Qin, D. Gao, W. Chen, Strong and tough antifreezing hydrogel sensor via the synergy of coordination and hydrogen bonds, ACS Appl. Mater. Interfaces 15 (2023) 51684–51693, https://doi.org/10.1021/acsami.3c10205.
[43] R. Liu, Y. Liu, S. Fu, Y. Cheng, K. Jin, J. Ma, Y. Wan, Y. Tian, Humidity adaptive antifreeze hydrogel sensor for intelligent control and human-computer interaction, Small 20 (2024) 2308092, https://doi.org/10.1002/smll.202308092.
[44] H. Ma, H. Qin, X. Xiao, N. Liu, S. Wang, J. Li, S. Shen, S. Dai, M. Sun, P. Li, X. Pan, M. Huang, B. Lu, J. Chen, L. Wu, Robust hydrogel sensors for unsupervised learning enabled sign-to-verbal translation, InfoMat 5 (2023) e12419, https://doi.org/10.1002/inf2.12419.
[45] J. Huang, X. Huang, P. Wu, One stone for three birds: one-step engineering highly elastic and conductive hydrogel electronics with multilayer MXene as initiator, crosslinker and conductive filler simultaneously, Chem. Eng. J. 428 (2022) 132515, https://doi.org/10.1016/j.cej.2021.132515.
[46] S. Han, Y. Hu, J. Wei, S. Li, P. Yang, H. Mi, C. Liu, C. Shen, A semi-interpenetrating poly(ionic liquid) network-driven low hysteresis and transparent hydrogel as a self-powered multifunctional sensor, Adv. Funct. Mater. 34 (2024) 2401607, https://doi.org/10.1002/adfm.202401607.